Agarose and Wax Tissue-Mimicking Phantom for Dynamic Magnetic Resonance Imaging of the Liver

Muntaser S. Ahmad[1], Osama Makhamrah[2], Nursakinah Suardi[3], Ahmad Shukri[3], Nik Noor Ashikin Nik Ab Razak[3] and Hjouj Mohammad[2]

[1]Department of Medical Imaging, Faculty of Applied Medical Health, Palestine Ahliya University, Jabal Daher PO Box 1041, Bethlehem. ZIP code 90907. West Bank, Palestine.

[2]Medical Imaging Department, Faculty of Health Professions, Al-Quds University, Abu Deis - Main Campus, 51000, Jerusalem, Palestine.

[3]School of Physics, Universiti Sains Malaysia, 11800, Penang, Malaysia.

ABSTRACT

Objectives: Polymer phantoms can be used to simulate the properties of tissues or organs such as the liver during magnetic resonance imaging (MRI). Although there are reports of simulated liver phantoms with hepatocellular carcinoma (HCC); no studies have documented the simulating of the typical dynamic pattern.

Aim: The present study aimed to investigate properties of developed phantoms with respect to the stability, including chemical, mechanical, electrical, as well as MRI properties (T1- and T2- signal intensities), in addition to simulating HCC in a dynamic way.

Methods: In this study, liver parenchyma of size 23 ×18 ×13 cm was simulated using three different agarose-wax samples (agarose at concentrations of 2.5 wt%, 4.5 wt%, and 6.0 wt%) mixed with a fixed wax concentration of 2.6 wt%.. HCC samples were fabricated using polyurethane and glycerol of various diameters (0.5, 1.0, and 2.0 cm).

Results: The results showed that the agarose-wax sample with a concentration of 2.5 wt% was the most stable sample among the other samples (P-value, 0.468) in mechanical and T1 and T2 intensities. It was also noted that the sample at the concentration of 4.5 wt% had the closest density value to human liver with a difference of 7.88%. Moreover, the agarose-wax sample at a concentration of 2.5 wt% had the closest compressibility and conductivity values, and T1-relaxation time compared to the human liver. However, the largest changes in relaxation times were observed in the fifth week of all samples (P-value = 0.047). The typical enhancement pattern for a simulated HCC of a minimum size, which can be measured with MRI, was 1.0 cm, using a body coil, and 0.5 cm using a head coil.

Conclusions: The chemical, electrical density, compressive strength, density, and MR imaging properties of the phantom were measured and compared to those of the human body.

Keywords
Magnetic Resonance Imaging, Hepatocellular carcinoma, Phantom.

Introduction
Hepatocellular carcinoma (HCC), a primary liver carcinoma, is classified as the third vital carcinoma in the world after lung and colorectal cancers [1]. It can be diagnosed using different imaging techniques, such as ultrasound, computed tomography (CT), and magnetic resonance imaging (MRI) [2]. MRI is the best modality for detecting HCC because of its ability to distinguish between contiguous tissues; providing highest value of signal-to-noise (SNR) and contrast-to-noise (CNR) [2]. This imaging technique

has been used as a quantitative analytic method for the diagnosis, staging, and treatment monitoring of HCC [3]. The effectiveness of HCC treatment depends on early detection, which in turn depends on the lesion size. Lesions in the early stages of HCC are < 1 cm in size, while those in the advanced stages > 2 cm [4]. The life span of a patient increases by about 5 years if HCC is diagnosed in its early stages, compared to 3 months if it is detected in the advanced and terminal stages [2,4].

In MRI applications, T_1- and T_2-weighted images are considered essential sequences for diagnosing different diseases in the liver, such as liver cirrhosis [5], fatty liver [6], hepatic iron overload [7], and HCC [3]. Quantitative MRI sequences are utilized for the diagnosis, staging, and monitoring of HCC.

Researchers and medical practitioners need a tool that can be used in experiments prior to human trials to detect the various stages of HCC. The ideal characteristics of the tool are ease of usage, continuous availability, cost-effectiveness, and the ability to mimic biological tissue. Phantoms are used in many medical applications, such as in developing medical techniques, improving image quality with different imaging techniques, helping surgeons to improve their skills, and assisting in detecting various diseases [8,9]. A phantom should possess the characteristics of MRI applications in terms of chemical, mechanical, electrical, magnetic, and imaging properties, so as to simulate the various organs within the human body.

Additionally, an ideal MRI liver phantom should have certain desirable characteristics. It needs to be designed for quantitative evaluation of standard proton spin relaxation times (T_1, T_2) such that it can uniformly support relaxation times with the ability to change T_1 and T_2 independently. Furthermore, the phantom can be shaped into forms similar to human organs to be compatible with the MRI field and coils, thus permitting change in temperature variation with respect to T_1 and T_2. To minimize any deterioration of quality over a period of time, the phantom should be easily fabricated. It should also have the ability to simulate the heterogeneous distribution between disease samples and normal liver parenchyma [10,11].

Liver MRI phantoms have been used for various purposes. These include the development of new pulse sequences, calibration of MRI equipment, training for liver surgery, and needle-guided puncture of lesions [8,12]. In previous studies, a number of tissue-mimicking materials including gelatin [13], agar [14,15], polyvinyl alcohol (PVA) has been used to simulate liver tissue in MRI [16,17]. Another material that has been used is agarose [18-20].

The use of HCC phantoms for successfully simulating human liver has been reported. However, few reports of the previous phantoms mimic the dynamic pattern of HCC. A number of important parameters need to be considered for the success of a dynamic phantom, including the ability to transfer gadoxetic acid–contrast media from artery to vein through the sample. The substance of the sample should have the appearance of HCC, should allow interaction with the contrast material, and be removable without changing the structure. The phantom should also allow for the changing of the HCC samples without affecting other phantom components. Finally, the phantom should allow control of the contrast material using an automatic injector and suction device [21,22]. The most important characteristic of the dynamic phantom lies in its ability to transmit the contrast agent within the different study samples, which are usually diseases tissues, to estimate how those samples interact with this material, thereby enabling the diagnosis with high accuracy.

The present study aimed to simulate human liver parenchyma using MRI using Agarose-Wax tissue mimicking materials and dynamically simulating HCC to represent classic enhancement patterns in HCC samples of various sizes in order to distinguish between the different stages of HCC.

Materials and Methods
Phantom Design
Agarose-wax samples may be prepared using a microwave or boiling water bath. Boiling water bath was used in the study. The phantoms used were fabricated following methods described in previous studies [21-23]. The main difference between this article and previous articles is that agarose was used in the experiment instead of gelatin in previous studies. The preparation of three samples of liver parenchyma using agarose and wax material was carried out in three stages. The first stage was preparing the agarose solution, the second step was the preparation of the wax solution, and the third was the preparation of the hydroxyethyl cellulose (HEC) mixture solution.

In the first phantom, 2.5 wt% agarose powder (UltraPure™, Sigma-Aldrich, St Louis, MO) was used, while in the second and the third phantoms, 4.5 wt% and 6.0 wt% of agarose was used respectively. A 2.6 wt% concentration of paraffin wax powder (block form, white; Sigma-Aldrich) was used in all samples. Next, 2.6 wt% of HEC powder, 0.5 wt % of benzalkonium chloride (BZK), and 3.2 wt% propanediol were also added to the mixture. BZK was used for its antibacterial properties, propanediol was used as a solvent in the mixture, and water was used as a volume spreader. Three different HCC sizes, 2.0 cm, 1.5 cm, and 0.5 cm in diameter were filled in the cylinders inserted inside the prepared phantom as in previous experiments [21]. All three samples had a spherical shape, and their sizes were determined by the cylinder size. All samples were prepared from 95.0 wt% polyurethane and 5.0 wt% glycerol. Elasturan 6005/264 (BASF Polyurethanes GmbH, 100 parts by weight (pbw), and ISO 136/131, 20 pbw with 5.0 wt% glycerol were mixed by hand to form the HCC samples. Table 1 shows the concentrations of all the materials used to prepare the agarose-wax mixture.

Table 1: Content of agarose, wax, HEC, BZK, propanediol, and water in the three phantoms.

	Agarose (wt%)	Wax (wt%)	HEC (wt%)	BZK (wt%)	Propanediol (wt%)	Water (wt%)	HCC
st phantom	2.5	2.6	2.6	0.2	3.2	88.9	
Second phantom	4.5	2.6	2.6	0.2	3.2	86.9	95.0 wt% polyurethane + 5.0 wt% glycerol
Third phantom	6	2.6	2.6	0.2	3.2	85.4	

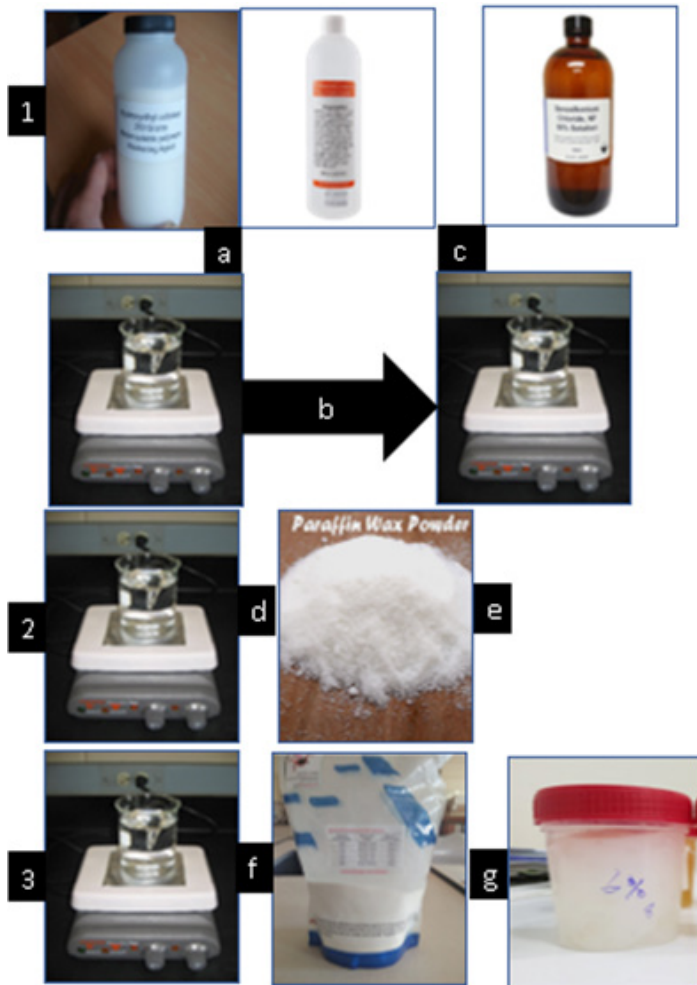HEC: Hydroxyethyl cellulose, BZK: Benzalkonium chloride, HCC: Hepatocellular carcinoma

Figure 1: General preparative steps of liver parenchyma made of agarose-wax mixture; (a) HEC powder and propanediol in 50 ml of water in the first beaker, heated to 140°C; (b) solution is cooled to 100°C; (c) BZK is added using a dropper; (d) paraffin wax powder in 50 ml of water in the second beaker, heated to 90°C; (e) solution in the first beaker is cooled to 90°C, and the wax solution from the second beaker is added; (f) agarose powder in 50 ml of water in the third beaker, heated to 50–60°C; (g) resultant solution from (e) is cooled to 60°C, and agarose solution is added.

Figure 1 depicts the entire preparation process for the agarose-wax mixtures. In the first stage of preparation, agarose (2.5 g) was dissolved in 50 ml of water for the first sample, 4.5 g of agarose in 50 ml for preparing the second sample, and 6 g of agarose in 50 ml of water to prepare the third sample. The three solutions were prepared in beakers, placed on a magnetic stirrer with the required amount of agarose powder slowly sprinkled into the beaker so that the solution was mixed to prevent the formation of agarose clumps. The beakers were heated to a temperature of 50–60°C for approximately 10 min until the agarose dissolved completely.

In the second phase, HEC powder (2.6 g) was added to 3.2 ml of propanediol in 50 ml of water. The solution was heated to 140°C and stirred using a magnetic stirrer. The solution was allowed to cool below 100°C before adding 0.2 ml of BZK using a dropper. The solution was continuously stirred to prevent gravitational sedimentation of the HEC particles. The third stage involved dissolving 2.6 g of paraffin wax powder in 50 ml of water. The solution was heated to 80–90°C and continuously stirred to prevent gravitational sedimentation of the wax powder particles.

Because of the different melting points of the agarose and wax solutions, the two solutions were prepared in separate beakers. Each container was heated to a different temperature until agarose and wax dissolved in the solution. Agarose reaches melting point at 40–60°C, whereas wax dissolves at 40–90°C. Temperature was monitored using a digital thermometer. After adding HEC, the mixture was allowed to cool to 90°C. The wax solution was then added, and the solution was continuously stirred to prevent sedimentation of HCE. The mixture was then allowed to cool to below 60°C before adding the agarose solution, again with continuous stirring. When the mixture reached 30°C, it was poured into a plastic container and stored at room temperature until use (Figure 1g).

A commercial liver mold made of polyvinyl chloride (PVC) with dimensions 23 ×18 ×13 cm was used as the container for the mixture. The mold could withstand the temperature of the mixture without any change in its shape. The liver shape was simulated using this mold.

The simulation steps used in this study are similar to those followed in two previous studies [21,23], where the dynamic phantom was fabricated using PVC tubes to simulate the functionality of the vessels. Three different sizes of HCC samples were placed inside three cylinders, which were implanted inside the phantom.

Phantom Characterizations
Liver tissue-mimicking materials (TMMs) were classified according to their chemical, mechanical (density and compressive strength), and electrical properties (conductivity). The chemical properties of the three phantoms were examined using a Bruker Alpha Fourier transform infrared (FTIR) spectrometer. The density of the phantoms was measured by dividing the sample mass by

volume and comparing it with the density of the human body (1.03 g/cm^3). Density measurements were taken over six weeks to monitor any changes in the density of the sample. A period of six weeks was chosen because any changes that would occur thereafter are likely due to the effect on the characteristics of the phantom resulting from significant proliferation of bacteria. All phantoms were stored at room temperature. The density coefficient variation (CV) value was calculated by dividing the standard deviation of density by the mean obtained from all readings during the six-week durations.

The compressive modulus was measured using an Instron compression-testing machine (Instron 4464) with ASTM standards. Study samples were placed in a cylindrical disk with a diameter of 10 mm and a height of 16 mm. The disc was placed on the pressure test plate after the load was lowered to the sample gradually and slowly until it touched the surface of the sample. This process continued until the sample reached the highest tolerance, after which the compressive strength was measured. For the electrical properties, the dielectric material analyzer SPECTANO 100 was used to measure the conductivity of the samples. The process was performed by placing flat samples between two gold plates. The dielectric properties of the materials were measured within a frequency range of 5.0 µHz to 5.0 kHz.

Imaging Properties of Liver Phantoms with HCC Samples

All MRI examinations were performed using a 1.5-Tesla MR system (MAGNETOM Avanto, Siemens Healthcare, Erlangen, Germany) equipped with a 48-channel body phase-array coil. Fast-low angle shot (FLASH) T_1-weighted images were obtained with echo acquisition [repetition time/echo time (TR/TE), 170/4.75 milliseconds (ms; flip angle, 70°; matrix, 203 x 320; field of view, 380×320 mm; slice thickness, 6 mm)].

T_2-weighted imaging was performed using half-Fourier acquisition single-shot turbo spin echo imaging (HASTE) (TR/TE, 1300/91 ms; matrix, 198×256; FOV, 380×320 mm; slice thickness, 6 mm).

Dixon sequence T_1-weighted images (TR/TE, 6.8/2.39 ms; flip angle, 10°; matrix, 195×320; FOV, 380×263 mm; slice thickness, 3.0 mm) were acquired after contrast material administration (Dotarem®, Guerbet, Roissy CdG Cedex, France). The parameters set in each of the four images presented by the Dixon sequence were as follows: out-of-phase (OP), in-phase (IP), fat suppression (Fat Sup), and water suppression (water Sup). The Dixon sequence was used to determine the quantity of water and fat in the tissue.

The delay post contrast material administration for arterial phase (AP) imaging was determined using the bolus detection technique (CARE Bolus; Siemens Healthineers). The mean delay times for the AP, portal venous phase (PVP), and delay phase (DP) were 25, 70, and 180 s, respectively. Dotarem was administered intravenously by using a standard weight-based dose of 0.2 mL/kg at a rate of 2 mL/s, followed by a 20 mL saline flush.

The GUI Strados software was used to estimate the signal intensity for both T_1 and T_2 signal intensities. By selecting an elliptical shape with diameter 10 mm^2 as the region of interest (ROI), three different readings of the parenchyma phantom were measured. The average of these readings was calculated and used to estimate the signal intensity. Figure 2 shows the reading locations of the phantom.
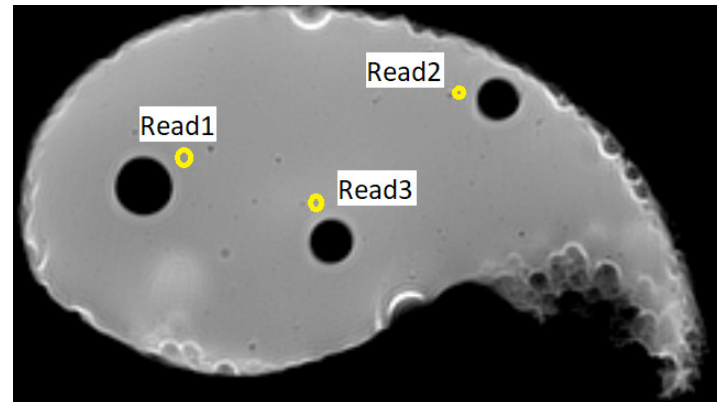

Figure 2: Reading locations of liver phantom for measuring signal intensities of T_1- and T_2-weighted image.

Effect of Post-fabrication Time on Phantom Stability on Signal Intensities of T_1WI and T_2WI

The stability of the samples was measured over six weeks. During this time interval, the viability of the sample materials was assessed using phantom materials. All three phantoms were measured for T_1W and T_2W signal intensities using the same parameters as mentioned above. All three phantoms were scanned once a week, and the positions were the same because the same position holder was used. Signal intensity coefficient variation values of T_1 and T_2 were calculated by dividing the standard deviation of the signal intensity by the mean readings during the six-week period.

Data analysis

Descriptive and frequency statistics were used to estimate the main characteristics of the samples. This included the mean, standard deviation, and percentages. Continuous variables were expressed as mean ± standard deviation. The independent-samples Kruskal-Wallis test was used to study the similarity of data between groups. Kruskal-Wallis test, or one-way ANOVA is used to compare two or more independent samples with different or equal sample sizes [24].

The Wilcoxon signed-rank test was used to study the changes with time over weeks within the same sample. *P-values* were used to check if there were any significant differences between the same sample using the Wilcoxon test.

Results
Phantom Characterizations
Chemical Properties of Liver Parenchyma Materials

Chemical analysis of the material is important because MRI depends on the atomic environment, which in turn depends on the chemical bonds within the material. Figure 3 shows that there are three clear peaks: the first peak at 1640 cm^{-1} corresponds to the

C=O stretch bond, followed by the CH_2 distribution profiles of wax across the agarose-wax peak at 2848 cm^{-1} wavenumber, and finally, the broadband peak at 3150–3350 cm^{-1} that represents the O-H stretch bond.
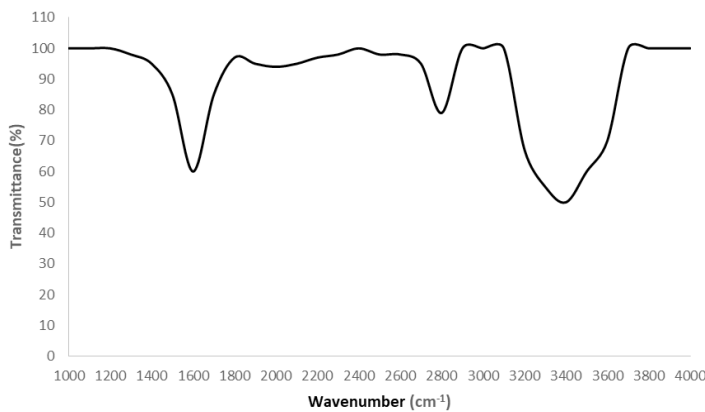

Figure 3: FTIR spectra of the agarose-wax liver tissue mimicking materials.

Mechanical Properties: Density, and Compressive Strength of agarose-wax Liver Parenchyma

The density CVs of the agarose-wax samples at different agarose concentrations are listed in Table 2. The table indicates that the density of agarose-wax samples was quite stable over the six-week period. The density at 4.5 wt% concentration was the closest to the real liver density; which is reported to be 1.03 g/cm^3. The density at this concentration ranged from 0.925 g/cm^3 to 0.95 g/cm^3; the difference from human density was 7.88% with a variation coefficient of 1.25%.

Table 2: Density changes in the agarose-wax samples with different agarose concentrations.

	W1	W2	W3	W4	W5	W6	CV	C.HL	P-value**
2.5wt%	110.7	111.4	111.4	111.4	111.4	111.1	0.26%	7.99%	0.468
4.5wt%	92.5	95.5	95.5	95.4	95.4	95	1.25%	7.88%	0.261
6.0wt%	113.6	115.5	115.4	115.4	115.3	114.9	0.63%	11.66%	0.388
P-value*	0.919	0.8757	0.878	0.879	0.882	0.885			

W: Week; CV: Coefficient variation; C. HL: Compared to human liver; P-value**: P-value within a group; P-value*: Significance between groups.

The results of the compressibility variation in the agarose-wax samples with different agarose concentrations and constant wax concentrations (2.6 wt%) are presented in Table 3. As seen from the table, the sample with 2.5 wt% agarose concentration had lowest compressibility values ranging from 0.093 to 0.16 MPa. It was noted that the compressibility of the three different concentrations of agarose-wax samples were comparable. The sample with 2.5 wt% of agarose-wax had the lowest compressibility value with an average of 0.109 MPa and a high CV value of 24.4%, and that with 6.0 wt% agarose-wax could be associated with the highest compressibility (average of 0.271 MPa) and a lower CV value of 9.99%.

Table 3: Variation of compression strength in the agarose-wax samples with different agarose concentrations.

	W1	W2	W3	W4	W5	W6	CV	P-value**
2.5wt%	0.098	0.12	0.16	0.095	0.092	0.093	24.4%	0.499
4.5wt%	0.12	0.15	0.13	0.16	0.11	0.13	13.96%	0.829
6.0wt%	0.23	0.29	0.27	0.25	0.3	0.29	9.99%	0.198
P-value*	0.234	0.228	0.464	0.000	0.284	0.220		

W: Week; CV: Coefficient variation; P-value**: P-value within a group; P-value*: Significance between groups.

In the fourth week, the differences between the three agarose-wax samples were apparent, with the P-value reaching 0.0000 (Table 3). The differences existed between the 2.5 wt% and 6.0 wt% samples as well as between the 4.0 wt% and 6.0 wt% samples with a P-value of 0.000 and 0.020, respectively. Agarose gel has a storage life of about 3-4 weeks if mixed with a specified amount of buffer solution. Therefore, in the fifth week, the differences in signal intensity readings was the greatest [25].

Electrical Properties of agarose-wax Liver Parenchyma

The variation of electrical conductivity in the agarose-wax samples relative to the different concentrations of agarose and a constant concentration of wax (2.6 wt%) is plotted in Figure 4. From this figure, it is evident that the conductivity of the agarose-wax samples increased with an increase in the concentration of agarose. The conductivity ranged from 0.678 to 0.922 mS/cm, 0.769 to 0.926 mS/cm and 0.788 to 0.929 mS/cm in the first, second, and third sample respectively.
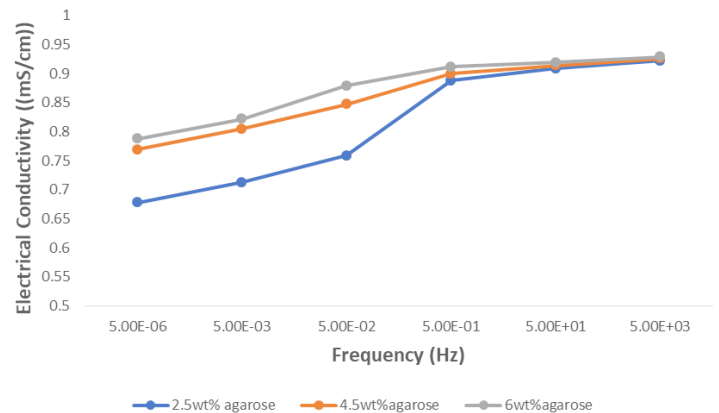

Figure 4: Electrical conductivity vs. frequency for agarose-wax samples.

The effect of agarose concentrations on relaxation times

Three different agaose concentrations were used to fabricate the liver phantom while the concentrations of the remaining components were fixed. The first phantom contained agarose concentration of 2.5 %wt, the second phantom contained 4.5 %wt of agarose, and the third phantom contained 6.0 %wt of agarose. Table 4 shows the effect of agarose concentrations upon the signal intensities T_1 and T_2.

Table 4: The effect of gelatin concentrations on relaxation times in agarose-wax samples.

	T_1 relaxation time ± SD (msec)	T_2 relaxation time ± SD (msec)
First phantom (2.5% of agarose)	193.25 ± 14.35	492.05 ± 22.93
Second phantom (4.5% of agarose)	196.41 ± 17.9	573.42 ± 24.81
Third phantom (6.0% of agarose)	197.86 ± 20.45	524.57 ± 21.56

Effect of Post-fabrication Time on Phantom Stability on the signal intensities of T_1- and T_2-weighted image signal intensity

The T_1-weighted image signal intensity changed by 8.68% (from 127 ms up to 165 ms) for the sample prepared from 2.5 wt% agarose, and the highest difference was found at week 5 with a variation of 12.12% (145-165). The CVs at the other two concentrations were more significant over time, especially for the sample prepared using 4.5 wt% concentration, where the CV reached 14.84% (from 103 ms up to 164 ms). While the signal intensity of the T_1-weighted image changed by 10.77% for the sample made with 6.0 wt% agarose concentration, significant differences in T_1 relaxation time were found over the six weeks at concentrations of 2.5wt% and 6.0 wt% (P-value, 0.003, and 0.031), respectively (Table 4). The differences in T_2 relaxation time over the same interval at 4.0 wt% agarose sample were significant (P-value = 0.006) (Table 5).

Table 4: Effect of time interval on signal intensities of T1-weighted imaging signal intensities in agarose-wax samples with different agarose concentrations.

	2.5 wt% agarose	4.5 wt% agarose	6.0 wt% agarose	P-value*
W1	127 ± 24	103 ± 10	121 ± 27	0.846
W 2	142 ± 22	152 ± 14	138 ± 25	0.821
W 3	140 ± 20	145 ± 18	146 ± 31	0.234
W 4	139 ± 19	139 ± 20	155 ± 21	0.333
W 5	145 ± 15	153 ± 25	152 ± 26	0.407
W 6	165 ± 14	164 ± 26	167 ± 28	0.546
CV	8.68%	14.84%	10.77%	
P-value**	0.031	0.078	0.003	

W: Week; CV: Coefficient variation; P-value**: P-value within a group; P-value*: Significance between groups.

Table 5: Effect of time interval on signal intensities of T_2-weighted imaging signal intensities in agarose-wax samples prepared using different agarose concentrations.

	2.5 wt% agarose	4.5 wt% agarose	6.0 wt% agarose	P-value*
W1	376 ± 45	100 ± 25	114 ± 11	0.362
W 2	472 ± 38	128 ± 26	182 ± 18	0.4266
W 3	464 ± 37	127 ± 29	184 ± 19	0.434
W 4	456 ± 41	127 ± 35	187 ± 21	0.443
W 5	461 ± 40	152 ± 30	164 ± 20	0.355
W 6	517 ± 49	163 ± 24	153 ± 35	0.318
CV	9.99%	16.65%	16.97%	
P-value**	0.069	0.006	0.596	

W: Week; CV: Coefficient variation; P-value**: P-value within a group; P-value*: Significance between groups.

Effect of gadoxetic acid–contrast medium on HCC

Since all HCC sample sizes were made from the same material (polyurethane combined with glycerol), the signal intensities for all samples were similar. Figure 5 shows the signal intensity of HCC samples in four different images (OP, IP, fat sup, and water sup) and at different imaging phases (pre-contrast, arterial, venous, and delay phases). All the images showed a similar trend with respect to the signal intensity and the imaging phases. During the pre-contrast phase, the signal intensities for all image types displayed the lowest values. However, after 25 s of contrast agent administration (arterial phase), the signal intensity reached its maximum value. In the venous phase, following 70s of contrast agent administration, the signal intensity decreased again. In the delay phase, after 180 s, where the gadoxetic acid–contrast medium was completely washed out, the signal intensity dropped to the lowest value. Relaxation times were calculated by taking a region of interest (ROI) within the HCC sample plotted in figure 6 at each of the selected delay times. The time-signal intensity curves were drawn by taking several different readings of the cancer samples over time. From these readings, the 25s, 70s, and 180s were selected to study the effect of contrast media on the HCC samples due to the fact that is taken in normal cases to depict the liver in a normal person.
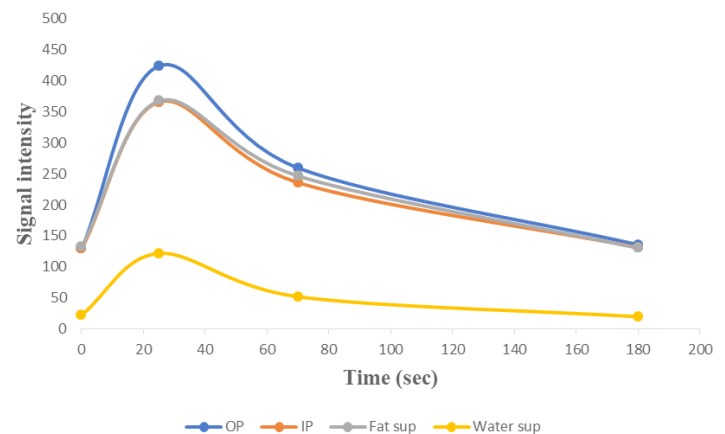

Figure 5: Time-signal intensity curves during gadoxetic acid–enhanced MR imaging through the first and second HCC samples (1.0 and 2.0 cm).

Figure 6 shows the behavior of the HCC samples following the application of gadoxetic acid–contrast media using a body coil. The three black spots inside the phantom were representative of the three cylinders containing the HCC samples (indicated by numbers 1, 2, and 3). The image shows three HCC samples with different sizes; sample 1 is 2.0 cm, sample 2 is 1.0 cm, and sample 3 is 0.5 cm [the sample images labeled as 1, 2, 3 in Figure 6(a)]. As seen in Figure 6(b), samples 1 and 2 appeared bright in color during the arterial phase before the contrast agent was injected into the liver phantom. However, the brightness decreased in the porto-venous phase [Figure 6(c)], before becoming black in the delay phase [Figure 6(d)] as in the pre-contrast phase. This is the typical pattern of HCC representation in the human body when it interacts with contrast media.
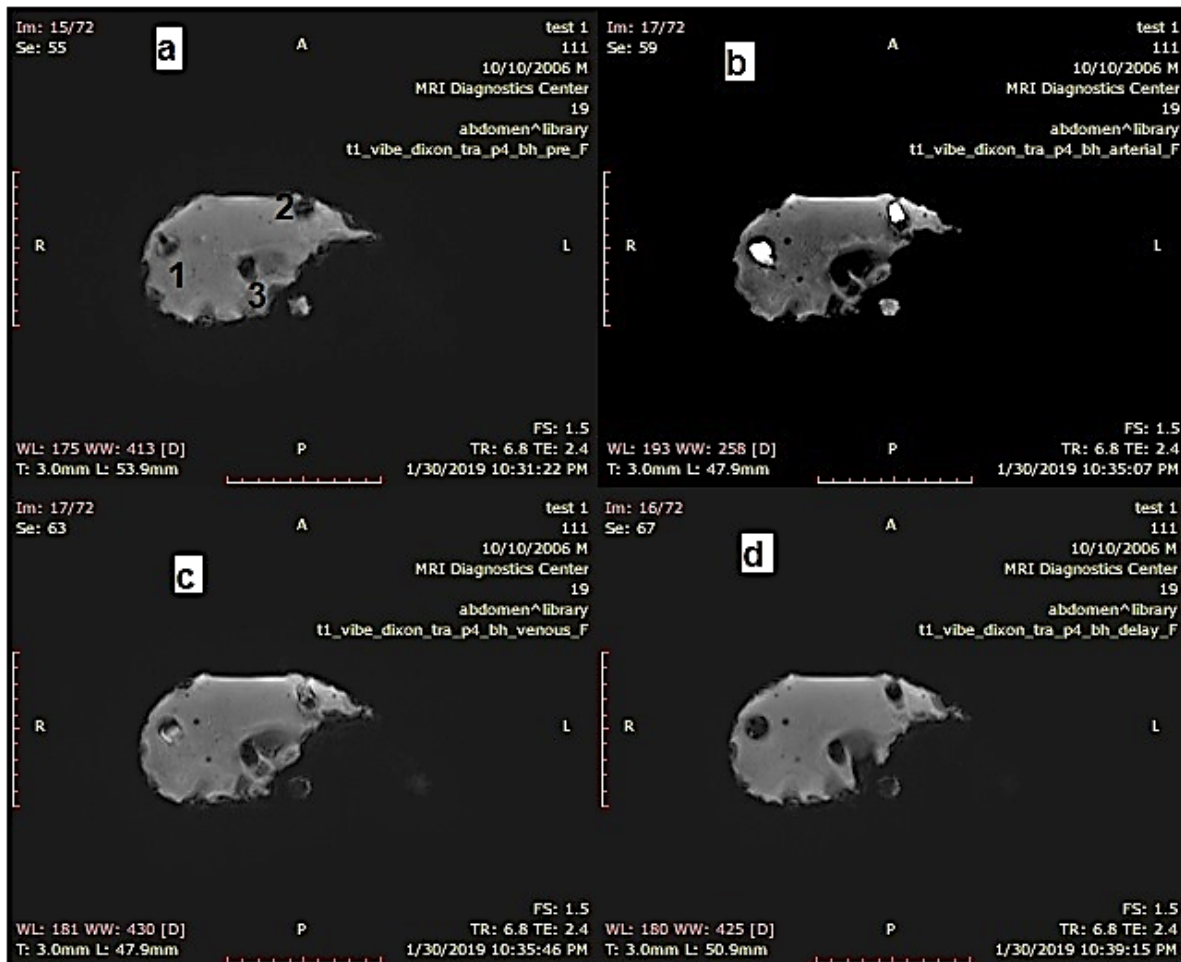
Figure 6: Dynamic application on HCC samples under Dixon's sequence; (a): pre-contrast image; (b): arterial phase image (AP); (c): porto-venous image; and (d): delay image.
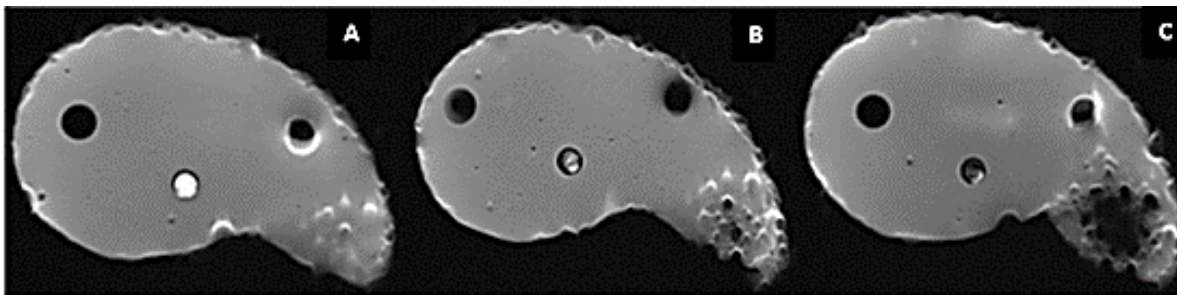

Figure 7: Dynamic phantom application on 0.5cm HCC sample using the head coil; (A): arterial phase image; (B): porto-venous phase image; and (C): delay phase image.

The stages of HCC depend on the size of the tumor itself [1,3]; the tumor size in the advanced stage is > 2.0 cm, in the middle stage it ranges between 1.0 and 2.0 cm, and in the earlier stage it is < 1.0 cm. In this study, these three stages of HCC stage are represented in samples 1, 2, and 3 respectively. As depicted in Figure 6, samples 1 and 2 of HCC can be easily detected by the body coil, while the smallest size (sample 3) does not appear in the image at any imaging phase. This is because the body coil was used as the signal receiver. The details and boundaries of the phantom image obtained using the body coil are not as clearly defined as those

of the phantom image obtained by the head coil. The head coil, type of volume coil, has a better homogeneity than the body coil (surface coil), which extends over a large area. The body coil is designed to receive signals from a large part of the body, such as the area around the abdomen, while the head coil is designed to receive signals from smaller parts of the body, such as the head region. Therefore, the dynamic phantom was applied to the 0.5 cm sample using a head coil at the same Dixon sequence parameters as it is more sensitive than the body coil. Even though the other two samples could have been visualized using a body coil, the

main advantage of using a head coil was to demonstrate its utility in viewing sample 3 despite the small sample size. Figure 7 shows the third HCC sample after the application of MRI contrast media.

Figures 6 and 7 demonstrate that by applying a dynamic phantom, the typical pattern of HCC appears as hyper arterial enhancement and delayed washout; the washout in porto-venous phase is typical for malignant lesions > 2.0 cm. These results are consistent with those reported in previous studies [26,27].

The amount of water and fat in the HCC samples was estimated using the time-signal intensity curve. It was expected that the percentage of water in the sample would be very large as the signal intensity in the water suppression (fat only) image showed a value of 22, while the signal intensity in the fat suppression (water only) image was 131. The signal intensity of HCC samples indicated that 52% of the HCC samples were made up of water and that 48% of the components were fat (glycerol and polyurethane).

As the fat percentage in the delay phase remained the same as in the pre-contrast phase, it can be stated that the materials used for fabrication of the HCC samples remained the same. However, there was a very small difference of 1% – 2% after the administration of contrast agent. This indicates that the contrast agent did not affect the components of the HCC sample.

Discussion

MRI phantoms have been used in routine calibration and to quantify the reliability of T_1 and T_2 measurements [28]. In the current study, we studied the possibility of creating a tissue-mimicking phantom to simulate MR relaxation times of liver tissue with HCC at 1.5-T using agarose-wax. The study showed that the chemical bonds between the three phantoms were similar. The 4.5 wt% concentration had the closest density value to real liver density, which is 1.03 g/cm³; whereas the 2.5 wt% concentration had the lowest value with an average of 0.109 MPa and a high CV value of 24.4%. The largest difference in the samples was seen with respect to the intensity of T_1 in the 6.0 wt% sample, whereas the 4.5 wt% sample showed the largest difference in intensity of T_2. Finally, the dynamics of the three HCC samples were simulated, and the early stages of HCC appeared during the use of the head coil, which were not visible by using the body coil.

As for the chemical properties, the C=O stretch bond important due to the dipole moment. Dipole moment are produced in the atom during the movement of the electrons, is constantly changing. Therefore, resonance susceptibility changes accordingly, and due to the greater appearance of this bond, a higher frequency is needed to obtain good signal intensities of T_1- and T_2-weighted images [29]. Likewise, the significance of the broad O-H stretch is to strengthen the hydrogen bond with the component molecules of the compounds, resulting in an increase in signal intensity in MRI [30]. The broadband peak refers to the water content in the samples. The peak width increased as the water content of the samples increased. Several reports have shown similar results with the same composition of gel-based TMMs through the use of carrageenan/agar and gelatin/agar gel samples [31].

While the density change in the samples can be explained by bacterial growth in the agarose-wax samples [32], the decrease in compressibility in samples with low agarose concentrations may be due to the reduction in the intermolecular bonds. In addition, low-concentration agarose samples have a large water content, which reduces compressibility [33,34]. From previous literature, it is known that the compressibility values of normal liver tissues ranges between 6.4 kPa and 60 kPa [34]. By comparing the compressibility of normal liver tissue, the sample composed of 2.5 wt% agarose combined with 2.6 wt% concentration of wax had an average compressibility of 0.109 MPa, which was the lowest value among all the samples. These results thus provide a higher magnitude of compressibility compared to human liver tissue. The reason for this was the percentage of water in the liver. The largest component of the liver is water or substances that are highly soluble in water, while the components of the various samples that were included in the study do not dissolve in water and, on the contrary, absorb water [35]. The lower compressibility at low concentrations of agarose can be explained by the reduced chemical bonds between the molecules in the sample [36]. In addition, low concentrations of agarose samples contain high water content, which reduces compressibility [33]. To achieve the desired compressibility of the human liver through the current phantom, a small amount of agarose should be used, reaching 1-1.5 wt%.

Electrical conductivity of phantom materials should be similar to that of the real human body because the magnetic field depends on magnetic homogeneity, which in turn relies on the wavelength of the mimicking tissue. The wavelength of the human body tissue, estimated as 0.99 cm, is less than that of air (468 cm). Hence, if the wavelength is different from the wavelength of the human tissue, the transmitted field will be affected by either constructive or destructive interference, resulting in the appearance of a bright image or signal loss [37]. Therefore, to achieve optimum calibration, electrical properties of TMMs should mimic those of human tissues. The conductivity of human body tissues is measured at frequencies ranging from 915 MHz to 2.45 GHz [37]. However, this frequency exceeds the usability of the device. Therefore, the results cannot be compared with those of the human liver. For this reason, the study focused on the effect of frequency on conductivity as well as the relationship of material concentrations in the samples based on the electrical conductivity.

Given the effect of a change in agarose concentration, agarose can be used as a T_1 and T_2 modifier. However, the change in T_2 was not statistically significant. This result is similar to those of previous studies [11,12,38,39]. While a majority of these reports demonstrated the effect of changes in agarose concentrations on T_2 signal intensity, the study of Kozana [28] demonstrated the effect of changes in agarose concentrations on both T_1 and T_2.

The difference in signal intensity of T_1-weighted image value for all concentrations was not significant, and the reason for this is that the agarose-wax samples have good stability in density over six weeks. Furthermore, as the addition of agarose to the samples limits the movement of water molecules within the sample, the movement of hydrogen spins is limited. Therefore, signal intensities of the three agarose-wax samples were comparable [40]. The effects of agarose concentration on the signal intensity of T_1-weighted images were similar to those obtained in a previous study by Yoshimura et al. [11], where the authors showed that the signal intensity of T_1-weighted images increases with the concentration of agarose.

The reason for the low signal intensity of T_2-weighted images in the agarose-wax samples is the use of agarose, which is used as a T_2 modifier on the one hand [40,41], and the use of wax as a T_2 modifier on the other [42,43]. The effect of agarose and wax in terms of T_2 modifier has the same effect as agar material, which is also used as a T_2 modifier [42]. As shown in Table 5, 2.5 wt% of agarose-wax concentration shows the most pronounced signal intensity of T_2-weighted images. This is because the content of water in this sample was greater than that in the other two samples. The signal intensity of T_2-weighted images mainly depends on the percentage of water in the sample. Thus, the signal intensity of the T_2-weighted image in agarose-wax at a concentration of 2.5 wt% is higher than that of the other two agarose-wax concentrations. For agarose concentrations of 4.5 wt% and 6.0 wt %, the signal intensity of T_2-weighted images in both samples was almost similar to the signal intensity of T_1-weighted images. This can be explained by the fact that increasing the agarose will increase the convergence of chemical bonds between the compositions [36], thereby reducing the signal intensity in the T_2-weighted image.

Typical HCC appears on MRI as hyperintensity in the arterial phase, hypointensity in the venous phase, and complete washout in the delay phase. These features mentioned in previous studies [44,45] as a classic HCC MRI pattern are consistent with the current experiment. The limitations of the current study lie in using a device that can measure electrical properties similar to the electrical properties of the human body.

Conclusion

For optimum phantom fabrication, mechanical, chemical, and electrical properties should be as stable as possible. Although each characteristic has its own significance, mechanical and physical properties are more important. However, the most critical one is the imaging property, as it correlates with the calibration accuracy and clinical relevance of the developed phantom. It is important to maintain phantom stability to simulate liver tissue. In this study, a dynamic liver phantom was used to simulate HCC at different stages. The results showed that early-stage HCC, expressed by a size of 0.5 cm, could not be explored using body coil in a distinctive way, but was detected using a head coil. Liver phantoms have been developed using several types of TMMs. This study found that the best material for the fabrication of liver phantom is agarose-wax, with an agarose concentration of 2.5 wt %, which is closest to real human liver in terms of mechanical and T_1 and T_2 relaxation times. Furthermore, it was confirmed that the TMM used here (polyurethane and glycerol) are capable of simulating HCC, and the results demonstrated that the samples interacted with the contrast agent and that this interaction did not change the composition of the sample itself. The current study can benefit from the clinical aspect, as it is possible to develop a Sequence-based on the head coil design for the early detection of HCC.

References

1. Ahmad MS, Suardi N, Shukri A, et al. Current status regarding tumour progression surveillance diagnosis staging and treatment of HCC a literature review. Journal of Gastroenterology and Hepatology Research. 2019; 8: 2841-2852.

2. European Association for The Study of The Liver. EASL clinical practice guidelines: management of hepatocellular carcinoma. Journal of hepatology. 2018; 69: 182-236.

3. Ahmad MS, Suardi N, Shukri A, et al. A recent short review in non-invasive magnetic resonance imaging on assessment of HCC stages MRI findings and pathological diagnosis. Journal of Gastroenterology and Hepatology Research. 2020; 9: 3113-3123.

4. Heimbach JK, Kulik LM, Finn RS, et al. AASLD guidelines for the treatment of hepatocellular carcinoma. Hepatology. 2018; 67: 358-380.

5. Petitclerc L, Sebastiani G, Gilbert G, et al. Liver fibrosis Review of current imaging and MRI quantification techniques. Journal of Magnetic Resonance Imaging. 2017; 45: 1276-1295.

6. Middleton MS, Van Natta ML, Heba ER, et al. Diagnostic accuracy of magnetic resonance imaging hepatic proton density fat fraction in pediatric nonalcoholic fatty liver disease. Hepatology. 2018; 67: 858-872.

7. Sheth S, Allen CJ, Farrell DE, et al. Measurement of the liver iron concentration in transfusional iron overload by MRI R2 and by high-transition-temperature superconducting magnetic susceptometry. Clinical imaging. 2019; 55: 65-70.

8. Rethy A, Sæternes JO, Halgunset J, et al. Anthropomorphic liver phantom with flow for multimodal image-guided liver therapy research and training. International journal of computer assisted radiology and surgery. 2018; 13: 61-72.

9. Surry KJ, Austin HJ, Fenster A, et al. Poly vinyl alcohol cryogel phantoms for use in ultrasound and MR imaging. Physics in Medicine & Biology. 2004; 49: 5529.

10. Ahmad MS, Suardi N, Shukri A, et al. Chemical characteristics motivation and strategies in choice of materials used as liver phantom a literature review. Journal of medical ultrasound. 2020; 28: 7.

11. Yoshimura K, Kato H, Kuroda M, et al. Development of a tissue-equivalent MRI phantom using carrageenan gel. Magnetic Resonance in Medicine an Official Journal of the International Society for Magnetic Resonance in Medicine. 2003; 50: 1011-1017.

12. Yoshida A, Kato H, Kuroda M, et al. Development of a phantom compatible for MRI and hyperthermia using carrageenan gel relationship between T 1 and T 2 values and NaCl concentration. International journal of hyperthermia. 2004; 20: 803-814.

13. Blechinger JC, Madsen EL, Frank GR. Tissue-mimicking gelatin agar gels for use in magnetic resonance imaging phantoms. Medical physics. 1988; 15: 629-636.

14. Kamel H, Syms RR, Kardoulaki EM, et al. Surgical wound monitoring by MRI with a metamaterial-based implanted local coil. EPJ Applied Metamaterials. 2018; 5: 5.

15. Bucciolini M, Ciraolo L, Lehmann B. Simulation of biologic tissues by using agar gels at magnetic resonance imaging. Acta Radiologica. 1989; 30: 667-669.

16. Gordon MJ, Chu KC, Margaritis A, et al. Measurement of Gd-DTPA diffusion through PVA hydrogel using a novel magnetic resonance imaging method. Biotechnology and Bioengineering. 1999; 65: 459-467.

17. Chu KC, Rutt BK. Polyvinyl alcohol cryogel an ideal phantom material for MR studies of arterial flow and elasticity. Magnetic resonance in medicine. 1997; 37: 314-319.

18. Gossuin Y, Burtea C, Monseux A, et al. Ferritin-induced relaxation in tissues an in vitro study. Journal of Magnetic Resonance Imaging an Official Journal of the International Society for Magnetic Resonance in Medicine. 2004; 20: 690-696.

19. Mitchell MD, Kundel HL, Axel L, et al. Agarose as a tissue equivalent phantom material for NMR imaging. Magnetic resonance imaging. 1986; 4: 263-266.

20. Christoffersson JO, Olsson LE, Sjöberg S. Nickel-doped agarose gel phantoms in MR imaging. Acta radiologica. 1991; 32: 426-431.

21. Ahmad MS, Suardi N, Shukri A, et al. Dynamic Hepatocellular Carcinoma Model Within a Liver Phantom for Multimodality Imaging. European journal of radiology open. 2020; 7: 100257.

22. Ahmad MS, Makhamrah O, Suardi N, et al. Hepatocellular Carcinoma Liver Dynamic Phantom For MRI. Radiation Physics and Chemistry. 2021; 109632.

23. Makhamrah O, Ahmad MS, Hjouj M. Evaluation of Liver Phantom for Testing of the Detectability Multimodal for Hepatocellular Carcinoma. In Proceedings of the 2019 2nd International Conference on Digital Medicine and Image Processing. 2019; 17-21.

24. Lou Y, Yuen SY, Chen G. Evolving benchmark functions using Kruskal-Wallis test. In Proceedings of the Genetic and Evolutionary Computation Conference Companion. 2018; 1337-1341.

25. Asuri P, Kunkel J. Function Structure and Stability of Enzymes Confined in Agarose Gels. PLoS One. 2014; 9: e86785.

26. Choi MH, Choi JI, Lee YJ, et al. MRI of small hepatocellular carcinoma typical features are less frequent below a size cutoff of 1.5 cm. American Journal of Roentgenology. 2017; 208: 544-551.

27. Ippolito D, Querques G, Okolicsanyi S, et al. Dynamic contrast enhanced perfusion CT imaging a diagnostic biomarker tool for survival prediction of tumour response to antiangiogenetic treatment in patients with advanced HCC lesions. European journal of radiology. 2018; 106: 62-68.

28. Kozana A, Boursianis T, Kalaitzakis G, et al. Neonatal brain Fabrication of a tissue-mimicking phantom and optimization of clinical T1w and T2w MRI sequences at 1.5 T. Physica Medica. 2018; 55: 88-97.

29. Wei W, Hu W, Zhang XY, et al. Analysis of protein structure changes and quality regulation of surimi during gelation based on infrared spectroscopy and microscopic imaging. Scientific reports. 2018; 8: 1-8.

30. Athokpam B, Ramesh SG, McKenzie RH. Effect of hydrogen bonding on the infrared absorption intensity of OH stretch vibrations. Chemical Physics. 2017; 488: 43-54.

31. Mohajer S, Rezaei M, Hosseini SF. Physico-chemical and microstructural properties of fish gelatin/agar bio-based blend films. Carbohydrate polymers. 2017; 157: 784-793.

32. Zhang YL, Liu Z, Liu T. Isolation and characterization of a novel paraffin wax-degrading bacterium Pseudomonassp strain PW-1 from petroleum-contaminated sites. Genet Mol Res. 2016; 15.

33. Buckley CT, Thorpe SD, O'Brien FJ, et al. The effect of concentration thermal history and cell seeding density on the initial mechanical properties of agarose hydrogels. Journal of the mechanical behavior of biomedical materials. 2009; 2: 512-521.

34. Normand V, Lootens DL, Amici E, et al. New insight into agarose gel mechanical properties. Biomacromolecules. 2000; 1: 730-738.

35. Gabriel S, Lau RW, Gabriel C. The dielectric properties of biological tissues II. Measurements in the frequency range 10 Hz to 20 GHz. Physics in medicine & biology. 1996; 41: 2251.

36. Oladzadabbasabadi N, Ebadi S, Nafchi AM, et al. Functional properties of dually modified sago starch/κ-carrageenan films an alternative to gelatin in pharmaceutical capsules. Carbohydrate polymers. 2017; 160: 43-51.

37. Roberts JJ, Martens PJ. Engineering biosynthetic cell encapsulation systems. In Biosynthetic Polymers for Medical Applications. Woodhead Publishing. 2016; 205-239.

38. Bitar R, Leung G, Perng R, et al. MR pulse sequences what every radiologist wants to know but is afraid to ask. Radiographics. 2006; 26: 513-537.

39. Ohno S, Kato H, Harimoto T, et al. Production of a human-tissue-equivalent MRI phantom optimization of material heating. Magnetic Resonance in Medical Sciences. 2008; 7: 131-140.

40. Kato H, Kuroda M, Yoshimura K, et al. Composition of MRI phantom equivalent to human tissues. Medical physics. 2005; 32: 3199-3208.

41. Hellerbach A, Schuster V, Jansen A, et al. MRI phantoms are there alternatives to agar. PloS one. 2013; 8: e70343.

42. Chmarra MK, Hansen R, Mårvik R, et al. Multimodal phantom of liver tissue. PloS one. 2013; 8: e64180.

43. Pluymen LH. Liver tissue mimicking materials for image-guided needle interventions. Master thesis TU Delft. 2016.

44. Matoori S, Roveri M, Tiefenboeck P, et al. An MRI-guided HIFU-triggered wax-coated capsule for supertargeted drug release a proof-of-concept study. European radiology experimental. 2019; 3: 11.

45. Ahmad MS, Makhamrah O, Hjouj M. Multimodal Imaging of Hepatocellular Carcinoma Using Dynamic Liver Phantom. 2021.